

Space Partitioning RANSAC

Daniel Barath

Department of Computer Science, ETH Zurich

danielbela.barath@inf.ethz.ch

Gabor Valasek

Eötvös Loránd University, Budapest

valasek@inf.elte.hu

Abstract

A new algorithm is proposed to accelerate RANSAC model quality calculations. The method is based on partitioning the joint correspondence space, e.g., 2D-2D point correspondences, into a pair of regular grids. The grid cells are mapped by minimal sample models, estimated within RANSAC, to reject correspondences that are inconsistent with the model parameters early. The proposed technique is general. It works with arbitrary transformations even if a point is mapped to a point set, e.g., as a fundamental matrix maps to epipolar lines. The method is tested on thousands of image pairs from publicly available datasets on fundamental and essential matrix, homography and radially distorted homography estimation. On average, it reduces the RANSAC run-time by 41% with provably no deterioration in the accuracy. It can be straightforwardly plugged into state-of-the-art RANSAC frameworks, e.g. VSAC.

1. Introduction

The RANSAC (RANdom SAMple Consensus) algorithm, proposed by Fischler and Bolles [13] in 1981, has become the most widely used robust estimator in computer vision. RANSAC and its variants have been successfully applied in a wide range of vision applications, such as short baseline stereo [37,39], wide baseline matching [24,25,29], performing [3,45] or initializing multi-model fitting algorithms [17,27], image mosaicing [15], detection of geometric primitives [34], pose-graph initialization for structure-from-motion pipelines [32,33], motion segmentation [37].

Briefly, RANSAC repeatedly selects random minimal subsets of the data points and fits a model to them, e.g., a 3D plane to three points, an essential matrix to five 2D point correspondences, or a rigid transformation to three 3D point correspondences. The quality of the model is then measured, for instance, as the cardinality of its support, i.e., the number of data points closer than a manually set inlier-outlier threshold. Finally, the model with the highest quality, refined, e.g. by least-squares fitting on all inliers, is returned. In this paper, we focus on speeding up the model

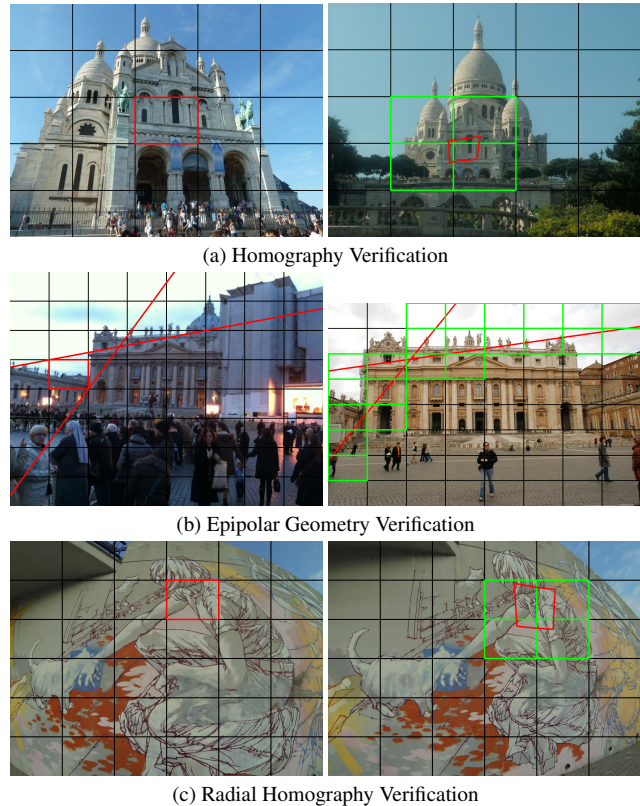


Figure 1. Examples of the proposed space partitioning-based model verification, i.e., quality calculation. For a particular cell in the left image (red rectangle), only those correspondences are considered where the point is in the rectangle and its corresponding pair falls inside one of the grid rectangles in the right image.

quality calculation via partitioning the correspondences into pairs of n -dimensional cells and we select the potential inliers extremely efficiently before computing the quality of each candidate model.

Since the introduction of RANSAC, a number of modifications have been proposed, replacing the components of the original algorithm. Many algorithms focus on improving the model accuracy via applying local optimization [2, 4, 5, 11, 21] that takes an initial model with rea-

sonably high quality and improves its parameters by, *e.g.* iterated least-squares fitting. To further increase accuracy, different model quality calculation techniques have been investigated by better modeling the noise in the data [36, 38] or marginalizing over the noise scale [4, 5].

To speed up the robust estimation procedure, several sampling algorithms have been introduced, increasing the probability of selecting a good sample early and, thus, triggering the termination criterion. The NAPSAC [35] sampler assumes that inliers are spatially coherent. It draws samples from a hyper-sphere centered on the first, randomly selected, location-defining point. The GroupSAC algorithm [26] assumes that inliers are often “similar” to each other and, thus, data points can be separated into groups according to their similarities. PROSAC [9] exploits an a priori predicted inlier probability rank of each point and starts the sampling with the most promising ones. P-NAPSAC [4] merges the advantages of local and global sampling by drawing samples from gradually growing neighborhoods.

Another way of making the procedure more efficient is to avoid unnecessary calculations when computing the quality of a candidate model. In most of the robust estimators, the quality calculation is done for every estimated model by computing *all* point-to-model residuals. In general, this procedure is of $\mathcal{O}(NK)$ complexity, where N is the number of input data points and K is the number of models generated inside RANSAC. In the case of having thousands of input data points or a low inlier ratio, the quality calculation dominates the run-time of the robust estimation.

A number of preemptive model verification strategies have been proposed to interrupt the model quality calculation when the probability of the current model being better than the previous best falls below a threshold. For example, when using the $T_{D,D}$ test [8], the model verification is first performed on D randomly selected points (where $D \ll N$). The remaining $N - D$ ones are evaluated only if the first D points are all inliers. The test was extended by the so-called bail-out test [7]. Given a model to be scored, a randomly selected subset of D points is evaluated. If the inlier ratio within this subset is significantly smaller than the current best inlier ratio, it is unlikely that the model will yield a larger consensus set than the current best and, thus, is discarded. In [10, 23], an optimal randomized model verification strategy was described. The test is based on Wald’s theory of sequential testing [42]. Wald’s SPRT test is a solution of a constrained optimization problem, where the user supplies acceptable probabilities for errors of the first type (rejecting a good model) and the second type (accepting a bad model) and the resulting optimal test is a trade-off between the time to decision and the errors committed.

These methods, however, do not exploit that in computer vision the estimated model is usually an $\mathbb{R}^n \rightarrow \mathbb{R}^m$ mapping defined on geometrically interpretable data points,

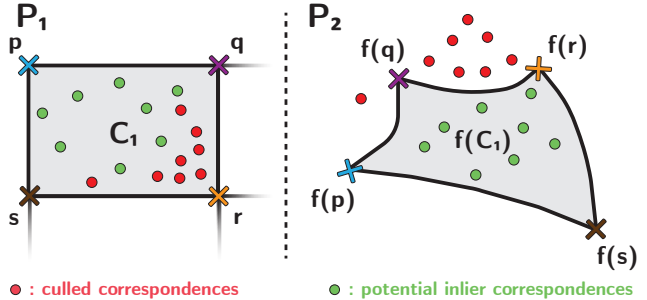


Figure 2. Cell C_1 in image plane P_1 and its projection $f(C_1)$ by model f to P_2 . Correspondences with their points in P_2 falling outside $f(C_1)$ are rejected (red dots). The potential inliers (green dots) of f are the ones that fall inside both C_1 and its image $f(C_1)$.

such as 2D-2D point correspondences. This property allows us to partition the input points by bounding structures, *e.g.* n -dimensional axis-aligned boxes (AABB), and to define the sought model as a mapping between the bounded domains. This is an extremely efficient way of selecting candidate inliers without calculating the point-to-model residuals of the rejected points. The benefit is two-fold: first, significantly fewer points are needed to be tested when calculating the model quality. Second, it allows an early model rejection if the number of selected candidate inliers is lower than that of the so-far-the-best model. Moreover, the proposed algorithm is *general*. It works for all kinds of models used in computer vision, *e.g.*, rigid motion, homography, epipolar geometry. It can be straightforwardly included in state-of-the-art frameworks, *e.g.* VSAC [18], and be combined with its “bells and whistles”, *e.g.* SPRT test [10, 23].

2. Background and Problem Formulation

Recent robust model fitting algorithms [2, 4–6, 18, 20, 30] spend a considerable amount of time calculating the point-to-model residuals when selecting the inliers of each verified model. The objective of this paper is to speed up the quality metric calculation by applying a conservative culling on the input point correspondences.

For simplicity, we first explain the idea through a simple example before formalizing it in a general way. Assume that we are given a homography, estimated from four point correspondences, and the objective is to calculate its support, *i.e.*, the number of inliers. As a preliminary step, we partition the points in each image to a regular grid, thus, having two grids in total. To determine the number of inliers, we process each cell of the first grid and check all (p, q) correspondences in them whether q is inside the projected image of the cell under the homography. More precisely, only those (p, q) correspondences are kept as candidate inliers, where q is in a cell in the second image which overlaps with the projection (by the homography) of the cell in which p

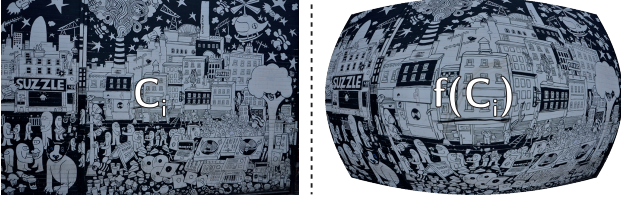


Figure 3. Image cell C_i and its projection $f(C_i)$.

falls. See Figures 1, 2 for examples.

General formulation. Let $\mathcal{S} = \{(\mathbf{p}_i, \mathbf{q}_i) \in \mathbb{R}^n \times \mathbb{R}^m \mid i = 1, \dots, N\}$ be a set of correspondences. \mathcal{S} may consist of 2D-2D point pairs found in two images and then used for estimating a homography or the epipolar geometry [16], 2D-3D correspondences used to solve the perspective- n -point problem [44], or 3D-3D ones for point cloud registration [28]. Let us assume that these correspondences stem from a ground truth $\mathbf{g} : \mathbb{R}^n \rightarrow \mathcal{P}(\mathbb{R}^m)$ mapping, perturbed by various sources of errors due to, *e.g.*, measurement and quantization. Note that \mathbf{g} may map a set of points to a single domain point, such as for essential matrices where an epipolar line is mapped to each point in the domain [16].

Our objective is to find an $\mathbf{f} : \mathbb{R}^n \rightarrow \mathcal{P}(\mathbb{R}^m)$ model mapping that best approximates \mathbf{g} in the sense that it produces a maximal inlier set for a given $\epsilon > 0$ inlier threshold. Formally, we seek the largest cardinality of the set

$$\mathcal{I}_{\mathbf{f}} = \{(\mathbf{p}_i, \mathbf{q}_i) \in \mathcal{S} \mid \exists \mathbf{q} \in \mathbf{f}(\mathbf{p}_i) : |\mathbf{q} - \mathbf{q}_i| < \epsilon\}, \quad (1)$$

where norm $|\cdot| : \mathbb{R}^m \rightarrow \mathbb{R}$ is some distance function defined on the points, *e.g.* re-projection error for homographies. This is the robust model fitting problem. Note that while our model quality function maximizes the inlier number, it is straightforward to use our proposed method with state-of-the-art functionals as well, such as the truncated quadratic loss of MSAC [38] or that of MAGSAC [5] and MAGSAC++ [4] marginalizing over a range of noise scale.

3. Correspondence Culling

Let $\mathcal{P}_1 \subset \mathbb{R}^n$ denote the domain of the $\mathbf{f} : \mathbb{R}^n \rightarrow \mathcal{P}(\mathbb{R}^m)$ model mappings and $\mathcal{P}_2 \subset \mathbb{R}^m$ the range. Our proposed method partitions the correspondences based on a spatial subdivision of \mathcal{P}_1 into cells. We show that the image of such regions may be conservatively bounded for a wide range of model mappings in the sense that it is guaranteed that no point of the cell may map outside of this bound. A $(\mathbf{p}_i, \mathbf{q}_i)$ correspondence is culled if $\mathbf{q}_i \in \mathcal{P}_2$ is outside of the bounded image of the cell containing $\mathbf{p}_i \in \mathcal{P}_1$. Alg. 1 summarizes our approach. The resulting set of correspondences is further processed by computing the exact inlier count.

Algorithm 1 Inlier prefiltering with conservative rejection

- 1: **Input:** model $\mathbf{f} : \mathbb{R}^n \rightarrow \mathcal{P}(\mathbb{R}^m)$; inlier threshold ϵ ;
 - 2: $\mathcal{C}_j, \mathcal{S}_j$ partitioning of \mathcal{P}_1 and \mathcal{S}
 - 3: **Output:** potential inliers \mathcal{I}
 - 4: $\mathcal{I} \leftarrow \emptyset$
 - 5: **for** $\forall C_j \in \mathcal{C}$ cell **do**
 - 6: $B \leftarrow \text{Bound}(\mathbf{f}(C_j), \epsilon)$
 - 7: **for** $\forall (\mathbf{p}_i, \mathbf{q}_i) \in \mathcal{S}_j$ **do**
 - 8: **if** $\mathbf{q}_i \in B$ **then**
 - 9: $\mathcal{I} \leftarrow \mathcal{I} \cup \{(\mathbf{p}_i, \mathbf{q}_i)\}$
 - 10: **end if**
 - 11: **end for**
 - 12: **end for**
-

3.1. Correspondence Partitioning

Let us partition \mathcal{P}_1 into a disjoint set of $C_j \in \mathcal{C}$ cells ($j \in \mathbb{N}_{>0}$) and store the correspondences based on these, *i.e.* let $\mathcal{S}_j = \{(\mathbf{p}_i, \mathbf{q}_i) \in \mathcal{S} \mid \mathbf{p}_i \in C_j\}$. In our particular case, we use a regular grid of equally sized axis-aligned rectangular cells for the subdivision. Partitioning is a pre-processing step with $\mathcal{O}(N)$ complexity and it only needs to be computed once, for example, upon reading the point correspondences. Decomposing \mathcal{S} into the \mathcal{S}_j partitions is not strictly necessary, however, it is an important component of efficient culling.

Note that the proposed method also allows using more advanced space partitioning algorithms, *e.g.*, quad-tree. We, however, found that the implied computational overhead is too large for the typical computer vision problems consisting, at most, of a few thousands of data points. This overhead stems from the tree construction and the increased number of cells to be projected by the proposed algorithm.

3.2. Culling by Images of Cells

The image of a cell depends on the current model \mathbf{f} and cannot be pre-computed. Consequently, we have to devise efficient means to compute or estimate this image, as it is calculated at every RANSAC iteration.

Invertible Case. Let us define the image of cell C_j as

$$\mathbf{f}(C_j) = \{\mathbf{y} \in \mathbb{R}^m \mid \exists \mathbf{x} \in C_j : \mathbf{y} \in \mathbf{f}(\mathbf{x})\}, \quad (2)$$

as shown in Figure 3. If there exists a closed-form of the generalized inverse mapping $\mathbf{f}^{-1}(\mathbf{y}) = \{\mathbf{x} \in \mathcal{P}_1 \mid \mathbf{y} \in \mathbf{f}(\mathbf{x})\}$, culling is trivial: a $(\mathbf{p}_i, \mathbf{q}_i) \in \mathcal{S}_j$ correspondence is culled, if and only if $\mathbf{f}^{-1}(\mathbf{q}_i) \notin C_j$. For example, if C_j is an axis-aligned bounding box, the test consists of four comparisons in 2D.

More generally, let us assume that C_j is written as the intersection of a finite number of

$$Q_{kj} = \{\mathbf{x} \in \mathcal{P}_1 \mid q_{kj}(\mathbf{x}) \leq 0\} \quad (3)$$

volumes, *i.e.* $C_j = \cap_k Q_{kj}$, where $q_{kj} : \mathcal{P}_1 \rightarrow \mathbb{R}$ is the implicit representation of the j -th boundary volume. Recalling that the intersection of implicitly defined volumes may be written as a maximum operation [31], a $(\mathbf{p}_i, \mathbf{q}_i) \in \mathcal{S}_j$ correspondence is culled, if and only if

$$\max\{q_{kj}(\mathbf{f}^{-1}(\mathbf{y}))\}_k > 0. \quad (4)$$

Thus, the containment test in the transformed space \mathcal{P}_2 is reduced to a containment test in \mathcal{P}_1 .

Although closed-form inversion is a strict restriction, all non-singular projective transformations possess this property. Moreover, since they are collineations, the line equations of the exact image may be used to carry out culling in \mathcal{P}_2 , however, culling against AABBs is more efficient.

General Case. If the inverse of \mathbf{f} is not available in closed-form, we may bound the image of cell C_j by using polynomial approximations to the exact transformed boundaries. We propose to use Lagrange interpolation at Chebyshev nodes to obtain these approximations.

This method assumes that the boundaries of the transformed cell, $\mathbf{f}(C_j)$, are the images of the cell boundaries in C_j , *i.e.*, $\mathbf{f}(\{\mathbf{x} \in \mathcal{P}_1 \mid q_{kj}(\mathbf{x}) = 0\})$. Once the polynomial approximations of the transformed boundary edges in \mathcal{P}_2 are obtained, we convert them to Bernstein basis [12] and use the convex hull of the control points to bound $\mathbf{f}(C_j)$. This is straightforward for models that map points to points as the polynomial approximations are traditional two or three dimensional Bézier curves. Models that map sets of points to points, *e.g.* epipolar geometry, can be embedded into this framework by assuming that the image sets are one parameter families and there exists a function basis that spans all sets. Formally, this means that, for all $\mathbf{x} \in \mathcal{P}_1$, we assume the existence of a $\mathbf{p}_\mathbf{x} : \mathbb{R} \rightarrow \mathcal{P}_2$ parametric mapping such that

$$\mathbf{f}(\mathbf{x}) = \{\mathbf{y} \in \mathcal{P}_2 \mid \exists t \in \mathbb{R} : \mathbf{y} = \mathbf{p}_\mathbf{x}(t)\}. \quad (5)$$

Let $\{e_i(t) : \mathbb{R} \rightarrow \mathbb{R}\}_{i=1}^k$ denote the basis that spans the images, *i.e.*, $\forall \mathbf{x} \in \mathcal{P}_1 : \forall i \in \{1, \dots, k\} : \exists \mathbf{a}_{\mathbf{x},i} \in \mathcal{P}_2 :$

$$\mathbf{p}_\mathbf{x}(t) = \sum_{i=1}^k \mathbf{a}_{\mathbf{x},i} e_i(t). \quad (6)$$

Then the polynomial approximation of the boundary is reduced to the construction of a higher dimensional Bézier curve that maps from \mathbb{R} to \mathbb{R}^{mk} , *i.e.* the Bézier curve is used to approximate the $\mathbf{a}_{\mathbf{x},i}$ coefficients. As shown in the example of epipolar geometry estimation, this can be made simpler for a particular problem.

Conservative Bounds. The polynomial approximations shown above can be made conservative by applying the Lagrange interpolation error term to them.

If an arbitrary boundary curve of cell C_j is parametrized over an interval $[a, b]$ by some $\mathbf{q}_{kj} : [a, b] \rightarrow \mathcal{P}_1$ ($k \in$

$\{1, 2, 3, 4\}$) mapping, then interpolating $\mathbf{f} \circ \mathbf{q}$ at k Chebyshev nodes $\mathbf{f}(\mathbf{q}_{kj}(\mathbf{x}_l))$, where

$$\mathbf{x}_l = \frac{a+b}{2} + \frac{b-a}{2} \cos \frac{2l-1}{2k} \pi, l = 1, \dots, k \quad (7)$$

yields a polynomial that is within

$$\frac{1}{2^{k-1}k!} \left(\frac{b-a}{2}\right)^k \cdot \max_{\xi \in [a,b]} \|(\mathbf{f} \circ \mathbf{q})^{(k+1)}(\xi)\|_\infty \quad (8)$$

of a $(k+1)$ times continuously differentiable $\mathbf{f} \circ \mathbf{q}$ mapping [40]. Thus, offsetting the AABB of the Bézier control points by this value ensures that no points in C_j may map outside the AABB bounding the image $\mathbf{f}(C_j)$ of cell C_j .

The simplest case is when the cells are axis-aligned rectangles and the \mathbf{q}_{kj} boundaries are linear interpolations between the vertices of the edges. Algorithm 2 summarizes the construction of conservative bounds to the images in such a configuration. This has to be run once for each cell. For each edge of the cell, it requires k evaluations of \mathbf{f} . Steps 6 and 7 can be carried out simultaneously by a multiplication of a $(k-1) \times (k+1)$ matrix with a $(k+1) \times 2$ matrix. Step 13 depends on the candidate mapping family. In the case when no closed-form solutions are available for the bound, one has to estimate it by numerical means. The bound on the image can be made tighter by using the second grid on \mathcal{P}_2 and select the cells that intersect the convex hull of the control points.

Note that, when using regular grids, the proposed algorithm can be significantly sped up by projecting the boundaries shared by multiple cells only once.

3.3. Early Model Rejection

The proposed approach provides all cell correspondences that might contain inliers of the currently estimated model. Besides being extremely useful for the verification, it also helps in rejecting models early without calculating their quality. The total number of data points stored in the selected cells is basically an upper bound on the inlier number. In the case this bound does not exceed the inlier number of the previous so-far-the-best model, the current model can be immediately rejected as it will not have more inliers than the best model so far. Therefore, a model θ is rejected if $\epsilon_r |\mathcal{I}^*| > |\mathcal{I}_\theta|$, where \mathcal{I}^* and \mathcal{I}_θ are, respectively, the inlier sets of the so-far-the-best and the currently tested models. Parameter $\epsilon_r = 1$ provably leads to no accuracy change. However, in practice, ϵ_r can be set marginally higher as we will show in the experiments.

Note that this approach works for all quality functions where the model quality is calculated from points closer than a manually set threshold, *e.g.*, as in RANSAC, MSAC or even in MAGSAC++ which uses a maximum threshold.

Algorithm 2 Bound($\mathbf{f}(C_j), \epsilon$) with AABB

Input: current candidate mapping $\mathbf{f} : \mathbb{R}^2 \rightarrow \mathcal{P}(\mathbb{R}^2)$;
approximation degree k ; C_j cell; $\epsilon > 0$

```

1:  $x_{min,j}, y_{min,j} \leftarrow +\infty$ 
2:  $x_{max,j}, y_{max,j} \leftarrow -\infty$ 
3: for  $\forall e$  edge of  $C_j$  do
4:    $\mathbf{a}, \mathbf{b} \leftarrow$  the endpoints of edge  $e$ 
5:    $\{\mathbf{x}_l \leftarrow \mathbf{a} + t_l(\mathbf{b} - \mathbf{a})\}_{l=1}^k$ ;  $t_l$  are Chebyshev nodes
6:    $\mathbf{c}(t) \leftarrow$  polynomial interpolating  $\{\mathbf{f}(\mathbf{x}_l)\}_{l=1}^k$ 
7:    $\mathbf{b}_0, \dots, \mathbf{b}_{k+1} \leftarrow$  Bézier control points of  $\mathbf{c}(t)$ 
8:    $x_{min,j} \leftarrow \min \{x_{min,j}, \min_{i=0}^{k+1} \{[1, 0] \cdot \mathbf{b}_i\}\}$ 
9:    $y_{min,j} \leftarrow \min \{y_{min,j}, \min_{i=0}^{k+1} \{[0, 1] \cdot \mathbf{b}_i\}\}$ 
10:   $x_{max,j} \leftarrow \max \{x_{min,j}, \max_{i=0}^{k+1} \{[1, 0] \cdot \mathbf{b}_i\}\}$ 
11:   $y_{max,j} \leftarrow \max \{y_{min,j}, \max_{i=0}^{k+1} \{[0, 1] \cdot \mathbf{b}_i\}\}$ 
12: end for
13:  $M \leftarrow$  bound on  $\|\mathbf{f}^{(k+1)}(\mathbf{a} + t(\mathbf{b} - \mathbf{a}))\|_\infty, t \in [0, 1]$ 
14:  $C \leftarrow \max_{\mathbf{x}} \prod_{j=0}^k |x - t_j| = \frac{1}{2^{2k-1}k!}$ 
15:  $\delta \leftarrow \epsilon + \|\mathbf{b} - \mathbf{a}\|_\infty \cdot M + C$ 
16: return  $\left( \begin{bmatrix} x_{min,j} - \delta \\ y_{min,j} - \delta \end{bmatrix}, \begin{bmatrix} x_{max,j} + \delta \\ y_{max,j} + \delta \end{bmatrix} \right)$ 

```

4. Model Estimation Problems

We show how the previously described general algorithm is used in various computer vision tasks.

4.1. Homography Estimation

Given homography $\mathbf{H} \in \mathbb{R}^{3 \times 3}$, the implied relationship of the points in the two images is written as $\alpha \mathbf{H} \mathbf{x}_1 = \mathbf{x}_2$, where α is a scaling that is inverse proportional to the homogeneous coordinate. The implied mapping is as

$$\mathbf{f}_{\text{hom}}(\mathbf{x}) = \begin{bmatrix} f_u(\mathbf{x}) \\ f_v(\mathbf{x}) \end{bmatrix} = \begin{bmatrix} \mathbf{h}_1^T \mathbf{x} / \mathbf{h}_3^T \mathbf{x} \\ \mathbf{h}_2^T \mathbf{x} / \mathbf{h}_3^T \mathbf{x} \end{bmatrix},$$

where $\mathbf{h}_1, \mathbf{h}_2, \mathbf{h}_3 \in \mathbb{R}^3$ are the rows of \mathbf{H} , and $f_u(\mathbf{x}), f_v(\mathbf{x})$ are coordinate functions. Since \mathbf{H} maps lines to lines and we use a regular grid, the culling algorithm can be simplified to using the AABB of the cell corners projected by \mathbf{f}_{hom} . This is a degree-one polynomial approximation that is also exact.

4.2. Epipolar Geometry Estimation

Given fundamental matrix \mathbf{F} , the implied relationship of the points in the two images is written as $\mathbf{x}_2^T \mathbf{F} \mathbf{x}_1 = 0$, meaning that point \mathbf{x}_2 in the second image must fall on the corresponding epipolar line $\mathbf{l}_2 = [a_2 \ b_2 \ c_2]^T = \mathbf{F} \mathbf{x}_1$. To bound the problem, we can assume that our model maps to the angle of the epipolar line as follows:

$$\mathbf{f}_{\text{epi}}(\mathbf{x}) = \tan^{-1} \frac{b_2(\mathbf{x})}{a_2(\mathbf{x})}, \quad \mathbf{f}_{\text{epi}}^{-1}(\mathbf{x}) = \tan^{-1} \frac{b_1(\mathbf{x})}{a_1(\mathbf{x})},$$

where $\mathbf{l}_i(\mathbf{x}) = [a_i(\mathbf{x}) \ b_i(\mathbf{x}) \ c_i(\mathbf{x})]$ is the epipolar line implied by \mathbf{x} in the i th image. Given cell C_j containing the epipolar angles, it can be straightforwardly seen that

$$\mathbf{f}_{\text{epi}}(C_j) : [\min\{\alpha \in C_j\}, \max\{\alpha \in C_j\}] \rightarrow [\min\{\alpha \in \mathbf{f}_{\text{epi}}(C_j)\}, \max\{\alpha \in \mathbf{f}_{\text{epi}}(C_j)\}].$$

Due to the convexity of the problem and the used regular grid, it can be decomposed into two sub-problems. First, the min and max operations are performed only on the intersections of the boundaries, *i.e.*, the cell corners. Therefore, a cell is not culled if at least one epipolar angle implied by its corners fall inside interval $[\min\{\alpha \in \mathbf{f}_{\text{epi}}(C_j)\}, \max\{\alpha \in \mathbf{f}_{\text{epi}}(C_j)\}]$. Second, a cell is not culled if one of its boundary lines intersects with the epipolar lines implied by angles $\min\{\alpha \in \mathbf{f}_{\text{epi}}(C_j)\}$ and $\max\{\alpha \in \mathbf{f}_{\text{epi}}(C_j)\}$. This is a more efficient formulation of the problem than considering epipolar lines as point sets.

4.3. Radial Homography Estimation

We use the one-parameter division model [14], for modeling radial distortion, having the following form:

$$\mathbf{g}(\mathbf{x}, \lambda) = [u, \ v, \ 1 + \lambda(x^2 + y^2)]^T,$$

where $\mathbf{x} = [u, v]^T$. Given homography $\mathbf{H} = [\mathbf{h}_1, \mathbf{h}_2, \mathbf{h}_3]^T$ with rows $\mathbf{h}_1, \mathbf{h}_2, \mathbf{h}_3 \in \mathbb{R}^3$, the points in the images are related as

$$\lambda_2 \mathbf{g}(\mathbf{x}_2, \lambda_2) = \mathbf{H} \mathbf{g}(\mathbf{x}_1, \lambda_1),$$

where \mathbf{x}_i and λ_i are, respectively, the point and the distortion parameter in the i th image, $i \in [1, 2]$. This implies the following mapping function

$$\mathbf{f}_{\text{rad}}(\mathbf{x}) = [f_u(\mathbf{x}) \ f_v(\mathbf{x})]^T,$$

where $f_u, f_v : \mathbb{R} \rightarrow \mathbb{R}$ are coordinate functions as follows:

$$f_u(\mathbf{x}) = \frac{\mathbf{h}_1^T \mathbf{g}(\mathbf{x})}{\mathbf{h}_3^T \mathbf{g}(\mathbf{x})}, \quad f_v(\mathbf{x}) = \frac{\mathbf{h}_2^T \mathbf{g}(\mathbf{x})}{\mathbf{h}_3^T \mathbf{g}(\mathbf{x})}. \quad (9)$$

The conservative bounds described in the previous sections are calculated from (9). Visualizations are submitted in the supplementary material.

5. Experiments

In this section, we compare the proposed space partitioning-based model verification technique to the traditional one. We do not report model accuracy since the proposed verification technique leads to exactly the same number of inliers as verifying all data points. We also note that the proposed algorithm can be straightforwardly combined with the widely-used preemptive model verification techniques, *e.g.* Sequential Probability Ratio Test [10].

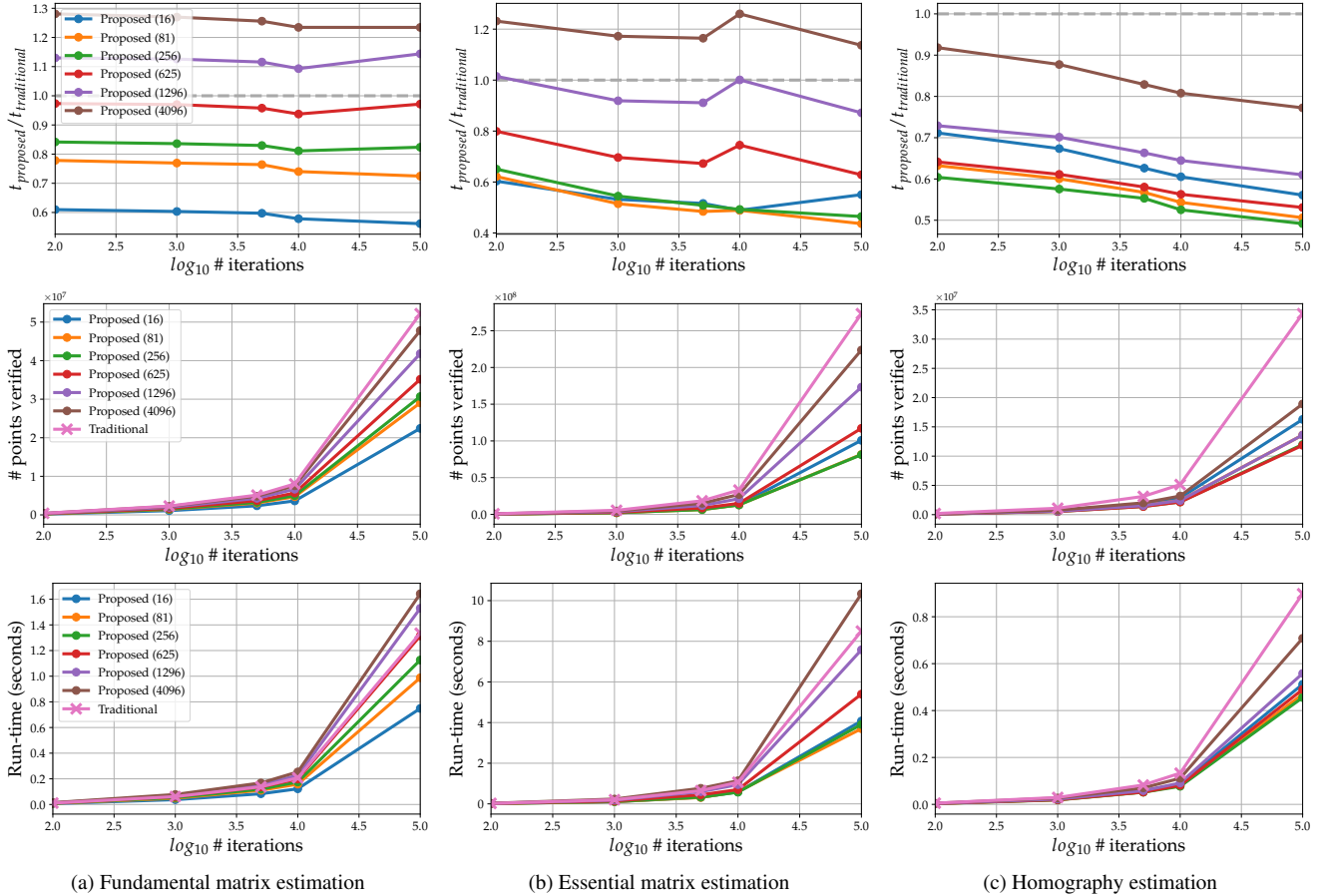


Figure 4. The ratio of times of the proposed and traditional methods (top row; vertical axis), the number of points verified within the RANSAC loop (middle) and the run-time in seconds (bottom) are plotted as a function of \log_{10} iteration number (horizontal). The number of 2D-2D cell pairs used in the proposed algorithm is written in brackets. For example, if the cell number is $2^4 = 16$, both images were divided into 2 pieces along each axis. We tested $2^4, 3^4, 4^4, 5^4, 6^4$, and 8^4 subdivisions running the algorithm on a wide range of cell sizes.

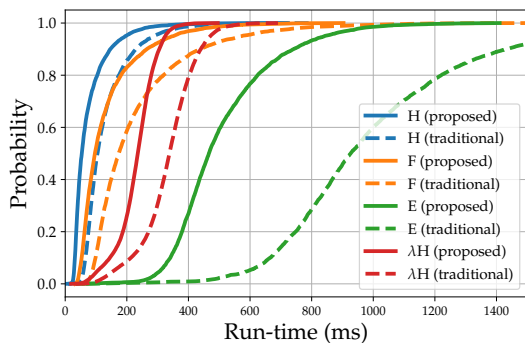


Figure 5. Cumulative distribution functions (CDF) of the times (in ms) of the proposed and traditional techniques on homography (H), fundamental (F) and essential matrix (E) estimation on 4950 image pairs, and radial homography estimation (λH) on 16056 pairs. Being fast is indicated by a curve close to the top-left corner.

5.1. Fundamental Matrix Estimation

For testing the methods on fundamental matrix estimation, we used the datasets from CVPR tutorial *RANSAC in 2020* [1]. The datasets and codes used are available at <https://github.com/ducha-aiki/ransac-tutorial-2020-data>. We used the inlier-outlier threshold for RANSAC tuned in [1]. We ran the method only on scene Sacre Coeur consisting of 4950 image pairs.

To form tentative correspondences, we detect 8000 SIFT keypoints in both images in order to have a reasonably dense point cloud reconstruction and precise camera poses [41]. We combine mutual nearest neighbor check with standard distance ratio test [22] to establish tentative correspondences, as recommended in [41].

In Fig. 4a, the relative run-time (*i.e.*, ratio of the time of the proposed and traditional approaches), the number of points verified in total and the processing time (in seconds) are plotted as the function of the \log_{10} iteration number –

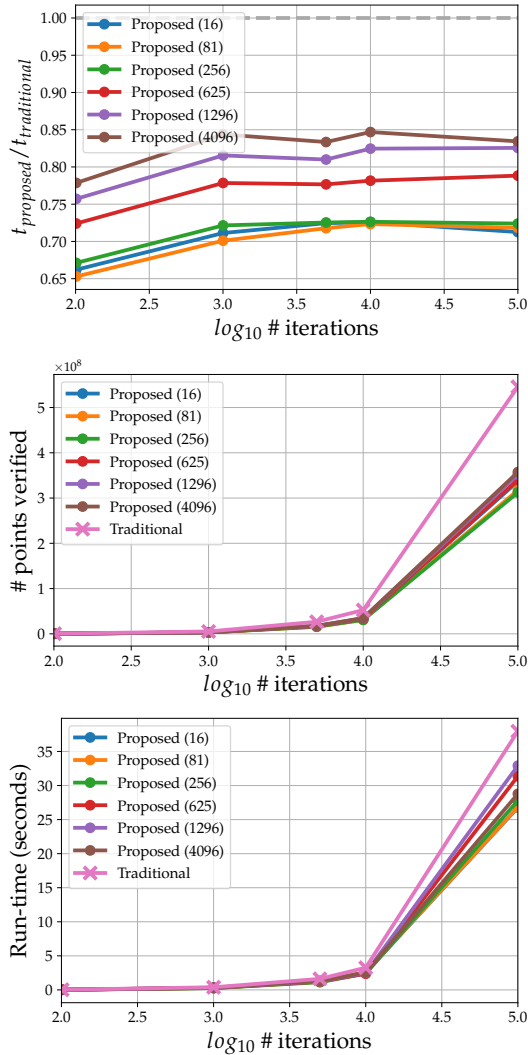


Figure 6. The ratio of run-times of the proposed and traditional methods (top row; vertical axis), the number of points verified (middle) and the actual run-time (bottom) are plotted as a function of \log_{10} iteration number (horizontal) for radial homography estimation on 16056 image pairs from the Sun360 dataset.

used as a fixed iteration number for RANSAC. The proposed early rejection was turned off for this experiment. Each curve shows the results of using a regular grid with different number of cells shown in brackets. For example, 16(= 2^4) means that each image axis is divided into 2 parts, thus, having 16 2D-2D cells in total. For fundamental matrix estimation, 16 cells lead to the fastest quality calculation with almost halving the run-time of the traditional approach. The time increases proportionally with the cell number. This is due to the fact that while having more cells provides a tighter approximation of the inlier set, it requires projecting more cells increasing the problem complexity. It is important to note that doing more RANSAC iterations

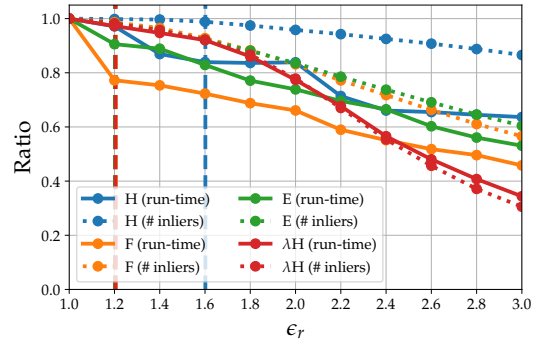


Figure 7. The change of run-times and inlier numbers plotted as the function of the early rejection threshold ϵ_r . The results are divided by the $\epsilon_r = 1$ case that provably does not lead to deterioration in the accuracy. The vertical lines are placed so the average drop in the inlier number is at most 1%.

becomes cheaper when the proposed method is used.

The orange curves in Fig. 5 show the cumulative distribution functions (CDF) of the processing times (in seconds) with and without the proposed technique. The results are calculated from the 4950 images pairs of scene Sacre Coeur. For this experiments, we run RANSAC with its confidence set to 0.99 and with a maximum iteration number of 5000. This maximum iteration number is a strict upper bound, preventing RANSAC to run longer. We set early rejection threshold ϵ_r to 1.2. The proposed approach almost halves the time of the entire robust estimation procedure.

5.2. Essential Matrix Estimation

For essential matrix estimation, we used the same data as for fundamental matrices. In Fig. 4b, the relative run-time, the number of verified points and the actual run-time are plotted as the function of the \log_{10} iteration number that was used as a fixed iteration number for RANSAC. Early rejection was turned off. Each curve shows the results of using a regular grid with different number of cells. Similarly as for fundamental matrix estimation, 16 cells lead to the fastest quality calculation. The speed-up is now even bigger: the run-time drops to its 40% when doing 10000 iterations. This is caused by the fact that the five-point solver returns a maximum of 10 candidate solutions – the same number of RANSAC iterations requires more models to be verified than for fundamental matrix estimation.

The green curves in Fig. 5 show the cumulative distribution functions of the processing times (in seconds) with and without the proposed technique. For this experiments, we run RANSAC with its confidence set to 0.99 and with a maximum iteration number of 5000. We set early rejection threshold ϵ_r to 1.2. It can be seen that the proposed approach causes a quite significant speed-up. RANSAC with grid-based quality calculation finishes in 1 second in almost

100% of the cases. Without the proposed approach, only 60% of the scenes finishes within 1 second.

5.3. Homography Estimation

For homography estimation, we used the same data as before. In Fig. 4c, the relative run-time is plotted as the function of the \log_{10} iteration number that was used as a fixed iteration number for RANSAC. Early rejection was turned off. Each curve shows the results of using a regular grid with different number of cells shown in brackets. The proposed approach leads to a speed-up with all tested cell numbers. In this case, 256 cells (each image is divided into 16 cells) lead to the fastest procedure. The run-time drops to its 50% when doing 10000 iterations, and it is significantly less dependent on the iteration number than for epipolar geometry estimation. This means that doing more iterations and, thus, likely increasing the accuracy is not that expensive when using the proposed algorithm.

The blue curves in Fig. 5 show the cumulative distribution functions of the processing times (in seconds) with and without the proposed technique. For this experiments, we run RANSAC with its confidence set to 0.99 and with a maximum iteration number of 5000. We set early rejection threshold ϵ_r to 1.6. The proposed approach almost halves the run-time in this experiment.

5.4. Radial Homography Estimation

To test the proposed techniques on real-world data, we chose the Sun360 [43] panorama dataset. The purpose of the Sun360 database is to provide academic researchers a comprehensive collection of annotated panoramas covering 360×180 -degree full view for a large variety of environmental scenes, places and the objects within. To build the core of the dataset, high-resolution panorama images were downloaded and grouped into different place categories. To obtain radially distorted image pairs from each 360° panoramic scene, we cut out images simulating a 80° FOV camera with a step size of 10° . Thus, the rotation around the vertical axis between two consecutive images is always 10° . Finally, image pairs were formed by pairing the consecutive images in each scene. In total, 16056 image pairs were generated. For estimating radial distortion homographies from minimal samples, we use the solvers from [19]. See Fig. 8 for an example image stitching using a radial homography on an image pair from the dataset.

The effect of the grid density is shown in Fig. 6. The proposed approach accelerates the robust radial homography estimation on the tested wide range of cell numbers. The best run-times are achieved by partitioning the images into 3 pieces along each axis and, thus, having 81 cell correspondences in total. The red curves in Fig. 5 show the cumulative distribution functions of the processing times (in seconds) with and without the proposed algorithm. We set



Figure 8. Radial homography in the Sun360 dataset [43].

early rejection threshold ϵ_r to 1.2. The proposed approach speeds up the estimation significantly.

5.5. Early Rejection

In Fig. 7, the change in the run-time and the final inlier number is plotted as the function of the early rejection threshold ϵ_r . The results are divided by the result of the $\epsilon_r = 1$ case that provably does not lead to deterioration in the accuracy. The vertical lines are placed so the rejection threshold leads to lower than 1% drop in the inlier number. The green, orange and red lines overlap. For homographies, $\epsilon_r = 1.6$ leads to negligible accuracy drop while further decreasing the run-time by approximately 20%. For all other tested problems, setting ϵ_r to 1.2 is a reasonable choice decreasing the processing time by 22% and 9%, respectively.

6. Conclusion

We propose a new general algorithm for accelerating the RANSAC model quality calculation. The method is based on partitioning the joint correspondence space to a pair of regular grids. Cells of the grids are then projected by each minimal sample model, before calculating the model quality, to efficiently reject all correspondences that are inconsistent with the model parameters. Besides speeding up the quality calculation significantly, it also allows us to reject models early if the upper bound of their inlier number does not exceed the inlier number of the so-far-the-best model. We found that dividing the domain, *e.g.* images, into a few cells is a good trade-off between getting a tight-enough approximation of the inlier set without significantly increasing the problem complexity.

The proposed technique reduces the RANSAC run-time by 41% on average on a wide range of problems and datasets. It can be straightforwardly inserted into any state-of-the-art robust estimator, *e.g.*, VSAC [18], to accelerate them without any negative side-effect.

Appendix A. Polynomial Approximation

This section gives a brief overview of three classic polynomial approximation schemes that we experimented with to bound the range of nonlinear transformations. The derivation of the results below are detailed in standard books on numerical analysis, we list these here for implementation reference and to make our paper self-contained. Similarly, we briefly summarize polynomial basis conversion via fitting for the sake of convenience.

The literature of polynomial approximations is rich, our selection of Taylor, Hermite, and Lagrange interpolation was motivated by ease of implementation and the existence and conciseness of error terms for these polynomials when used in the context of function approximation.

In terms of convenience, Lagrange interpolation in Bernstein basis is the least obtrusive solution as it only requires the evaluation of the target function. Hermite and Taylor expansions require higher order derivatives, which have to be either computed formally, via automatic differentiation, or numerical differentiation. However, all solutions require the ability to bound the magnitude of certain derivatives, if conservative bounds are to be computed.

A.1. Taylor Approximation

We denote the n -dimensional Euclidean space by \mathbb{R}^n and $\|\cdot\|_2$ is the Euclidean norm. The partial derivatives of an $f : \mathbb{R}^2 \rightarrow \mathbb{R}$ function are $\partial_1 f, \partial_2 f$ or f_x, f_y . The scalar product of vectors $\mathbf{a}, \mathbf{b} \in \mathbb{R}^n$ is written as $\langle \mathbf{a}, \mathbf{b} \rangle = \mathbf{a}^\top \mathbf{b}$.

Definition 1. Let $\boldsymbol{\alpha} = (\alpha_1, \dots, \alpha_n) \in \mathbb{N}^n$ be a multi-index. Then we define the following operations:

- $|\boldsymbol{\alpha}| = \alpha_1 + \alpha_2 + \dots + \alpha_n$
- $\boldsymbol{\alpha}! = \alpha_1! \cdot \alpha_2! \cdot \dots \cdot \alpha_n!$, where $0! = 1$
- $\mathbf{x}^\boldsymbol{\alpha} = x_1^{\alpha_1} \cdot x_2^{\alpha_2} \cdot \dots \cdot x_n^{\alpha_n}$ ($\mathbf{x} = (x_1, x_2, \dots, x_n) \in \mathbb{R}^n$)
- $\partial^\boldsymbol{\alpha} f = \partial_1^{\alpha_1} \partial_2^{\alpha_2} \dots \partial_n^{\alpha_n} f$ ($f : \mathbb{R}^n \rightarrow \mathbb{R}$)

Definition 2. Let $f : \mathbb{R}^n \rightarrow \mathbb{R}$ be $f \in C^{k+1}$. The degree k multivariate Taylor approximation of f about \mathbf{x}_0 is

$$T_{k, \mathbf{x}_0}(\mathbf{x}) = \sum_{|\boldsymbol{\alpha}| \leq k} \frac{\partial^\boldsymbol{\alpha} f(\mathbf{x}_0)}{\boldsymbol{\alpha}!} (\mathbf{x} - \mathbf{x}_0)^\boldsymbol{\alpha}. \quad (10)$$

Theorem 1 (Taylor Approximation Theorem). Let $f : \mathbb{R}^n \rightarrow \mathbb{R}, S \subset \mathbb{R}^n$ open and convex, $f \in C^{k+1}[S]$. If $\mathbf{a}, \mathbf{a} + \mathbf{h} \in S$, then

$$f(\mathbf{a} + \mathbf{h}) = T_f^{(k)}(\mathbf{a} + \mathbf{h}) + R_{\mathbf{a}, k}(\mathbf{h}) \quad (11)$$

where the residual $R_{\mathbf{a}, k}$ can be expressed using an adequate $c \in (0, 1)$:

$$R_{\mathbf{a}, k}(\mathbf{h}) = \sum_{|\boldsymbol{\alpha}| = k+1} \partial^\boldsymbol{\alpha} f(\mathbf{a} + c \cdot \mathbf{h}) \frac{\mathbf{h}^\boldsymbol{\alpha}}{\boldsymbol{\alpha}!} \quad (12)$$

or, with an integral form, as

$$R_{\mathbf{a}, k}(\mathbf{h}) = (k+1) \sum_{|\boldsymbol{\alpha}| = k+1} \frac{\mathbf{h}^\boldsymbol{\alpha}}{\boldsymbol{\alpha}!} \int_0^1 (1-t)^k \partial^\boldsymbol{\alpha} f(\mathbf{a} + t\mathbf{h}) dt. \quad (13)$$

Corollary 1.1 (Error bound of Taylor approximation). Let $f : \mathbb{R}^n \rightarrow \mathbb{R}$ be such that $f \in C^{k+1}[S]$ and $M > 0$ such that $\forall \mathbf{x} \in S : \forall |\boldsymbol{\alpha}| = k+1 : |\partial^\boldsymbol{\alpha} f(\mathbf{x})| \leq M$. Then

$$R_{\mathbf{a}, k}(\mathbf{h}) \leq \frac{M}{(k+1)!} \|\mathbf{h}\|_1^{k+1}. \quad (14)$$

In the two-dimensional case, the Taylor polynomials are written as

$$T_f^{(k)}(x, y) = \sum_{i=0}^k \sum_{j=0}^i \frac{\partial_1^j \partial_2^{i-j} f(a, b)}{j!(i-j)!} (x-a)^j (y-b)^{i-j} \quad (15)$$

In the case of vector valued functions of two variables, the Taylor expansion naturally generalizes to

$$\mathbf{T}_f^{(k)}(x, y) = \sum_{i=0}^k \sum_{j=0}^i \frac{\partial_1^j \partial_2^{i-j} \mathbf{f}(a, b)}{j!(i-j)!} (x-a)^j (y-b)^{i-j} \in \mathbb{R}^n \quad (16)$$

A.2. Hermite Interpolation

Definition 3 (Hermite interpolant). Let $f : \mathbb{R} \rightarrow \mathbb{R}$ be such that $f \in C^{k+1}$. The polynomial $h_k(x)$ of degree $2k+1$ is an order k Hermite interpolant at $a, b \in \mathbb{R}$ if and only if

$$h_k^{(i)}(a) = f^{(i)}(a) \quad (17)$$

$$h_k^{(i)}(b) = f^{(i)}(b) \quad (18)$$

holds, $i = 0, \dots, k$ and $f^{(i)}$ denotes the i -th derivative.

The above two-point Hermite interpolation is sometimes described as dense in the sense that all derivatives and function values are prescribed up to a fixed order and there are no gaps, that is, missing derivatives. It can be easily seen that the Hermite interpolation polynomial is unique. More importantly, its error characteristics are given by

Theorem 2 (Error bound of Hermite interpolation). Let $f : \mathbb{R} \rightarrow \mathbb{R}$ be such that $f \in C^{k+1}$ and let $h_k(x)$ be an order k Hermite interpolant at $a, b \in \mathbb{R}$. Then for all $x \in [a, b]$ exists a $\xi \in [a, b]$ such that

$$f(x) - h_k(x) = \frac{f^{(k+1)}(\xi)}{(k+1)!} (x-a)^k (x-b)^k. \quad (19)$$

Oftentimes, it is more convenient to bound the above as a function of the $b-a$ width of the domain. The maximum of the function is attained at the midpoint of the interval

and straightforward substitution gives the resulting modified bound. The above holds for vector valued functions as well but similarly to the Taylor case, the 1-norm has to be used.

In our case, we approximate the image of the cell boundary curves, thus the single variable error term is sufficient.

A.3. Lagrange Interpolation

By Lagrange interpolation we refer to the interpolation of a $f : [a, b] \rightarrow \mathbb{R}, [a, b] \subset \mathbb{R}$ function at some prescribed $a = x_0 < x_1 < \dots < x_k = b$ points by polynomials. Then the following holds

Theorem 3. *If $p_k(x)$ is a polynomial that interpolates $f : [a, b] \rightarrow \mathbb{R}, [a, b]$ at $a = x_0 < x_1 < \dots < x_k = b$ and $f \in C^{k+1}[a, b]$, then for any $x \in [a, b]$, there exists a $\xi \in (a, b)$ such that the following holds:*

$$f(x) - p_k(x) = (x - x_0) \cdots (x - x_k) \frac{f^{(k+1)}(\xi)}{(n+1)!}. \quad (20)$$

There are ways to re-phrase the above in terms of differences, should the target function not meet the continuity assumptions of the theorem but we did not experiment with the practical applicability of these.

As we have no control over the magnitude of $f^{(k+1)}(\xi)$, the only way to minimize the error in (20) is to find $x_i \in [a, b]$ nodes that minimize $\prod_{i=0}^k (x - x_k)$ over $[a, b]$.

Definition 4 (Chebyshev polynomials). *The Chebyshev polynomials over $[-1, 1]$ are defined recursively as*

$$T_0(x) = 1, \quad (21)$$

$$T_1(x) = x, \quad (22)$$

$$T_{k+1}(x) = 2xT_k(x) - T_{k-1}(x) \quad (23)$$

for $k \geq 1$.

Theorem 4 (Interpolation at Chebyshev nodes). *If $p_k(x)$ is a polynomial that interpolates $f : [-1, 1] \rightarrow \mathbb{R}, f \in C^{k+1}[a, b]$ at the roots of $T_{k+1}(x)$, that is, $x_i = \cos\left(\frac{2i+1}{2k+2}\right)$, $i = 0, 1, \dots, k$, then*

$$|f(x) - p_k(x)| \leq \frac{1}{2^k(k+1)!} \max_{t \in [-1, 1]} |f^{(k+1)}(t)|. \quad (24)$$

This is the best upper bound if we can only vary the location of the x_i interpolation nodes.

If the function is defined over an arbitrary $[a, b]$ interval, the Chebyshev nodes simply have to be affinely mapped from $[-1, 1]$ to $[a, b]$ to compute the necessary Chebyshev nodes as follows:

$$x_i = \frac{a+b}{2} + \frac{b-a}{2} \cos\left(\frac{2i+1}{2k+2}\right). \quad (25)$$

Appendix B. Bounding Polynomials

B.1. Properties of Bézier Curves

Let $\mathbf{b}_i \in \mathbb{R}^d, (i = 0, 1, \dots, n)$ denote the control points of a d -dimensional Bézier curve. The parametric equation of the curve is

$$\mathbf{b}(t) = \sum_{i=0}^n \mathbf{b}_i B_i^n(t), \quad t \in [0, 1], \quad (26)$$

where $B_i^n(t)$ are the Bernstein polynomials over $[0, 1]$, i.e.

$$B_i^n(t) = \binom{n}{i} t^i (1-t)^{n-i}. \quad (27)$$

As the Bernstein basis is positive and forms a partition of unity (i.e. $B_i^n(t) \geq 0, t \in [0, 1]$ and $\sum_{i=0}^n B_i^n(t) = 1$), it follows that all points of the curve are contained within the convex hull of its \mathbf{b}_i control points. Consequently, the axis aligned bounding box of the control points is a conservative bound on the range of the curve.

Similarly, if we want to bound the magnitude of a $\mathbf{f} : \mathbb{R} \rightarrow \mathbb{R}^n$ vector valued function, we can construct a Bézier approximation to the $\|\mathbf{f}(x_i)\|$ magnitude values (in arbitrary norm) via interpolation and use the value of the largest control point (here, scalar) to infer an approximate upper bound on the magnitude.

B.2. Interpolating Data

Recall that the evaluation of a function in a basis such as in Equation (26) can be written in matrix form as

$$\mathbf{b}(t) = [B_0^n(t), B_1^n(t), \dots, B_n^n(t)] \cdot \begin{bmatrix} \mathbf{b}_0 \\ \mathbf{b}_1 \\ \dots \\ \mathbf{b}_n \end{bmatrix} \quad (28)$$

As such, when given $n+1$ parameter values $t_0 < t_1 < \dots < t_n$ and corresponding points in space $\mathbf{p}_0, \mathbf{p}_1, \dots, \mathbf{p}_n$, we can compute the $\mathbf{b}_i, (i = 0, 1, \dots, n)$ Bézier control points that interpolate them by solving

$$\begin{bmatrix} B_0^n(t_0) & B_1^n(t_0) & \dots & B_n^n(t_0) \\ B_0^n(t_1) & B_1^n(t_1) & \dots & B_n^n(t_1) \\ \dots & \dots & \dots & \dots \\ B_0^n(t_n) & B_1^n(t_n) & \dots & B_n^n(t_n) \end{bmatrix} \cdot \begin{bmatrix} \mathbf{b}_0 \\ \mathbf{b}_1 \\ \dots \\ \mathbf{b}_n \end{bmatrix} = \begin{bmatrix} \mathbf{p}_0 \\ \mathbf{p}_1 \\ \dots \\ \mathbf{p}_n \end{bmatrix} \quad (29)$$

for $[\mathbf{b}_0, \dots, \mathbf{b}_n]^T$. One can either use a linear solver for better robustness, or use interpolation nodes that yield a small condition number for the matrix on the left. Chebyshev nodes are such a choice, up to moderate degrees (that is, up to 10), making direct inversion possible which reduces the interpolation problem to a simple matrix-vector multiplication. Note that if $t_0 = 0, t_n = 1$, the first and the last

rows of the matrix are e_1, e_{n+1} respectively, where e_i are the canonical basis vectors of dimension $n + 1$.

In our tests on Lagrange interpolation, we used the roots of the Chebyshev polynomials over closed intervals, i.e. $t_i = \frac{1}{2} (1 - \cos(\frac{i\pi}{n})) \in [0, 1], i = 0, \dots, n$.

B.3. Converting Hermite to Bézier Control Data

Since we approximate our mapped boundary curves from endpoint derivative data, *i.e.* we use Hermite interpolation, we have to convert the Hermite basis polynomial data to Bernstein basis. This can be done by brute-force interpolation, as in evaluating the Hermite polynomial in $n + 1$ points and multiplying the resulting vector by the inverse of the Bernstein evaluation matrix of at the sample parameters, as shown in the previous subsection.

A simpler approach is possible, however, by recalling that the derivatives of Bézier curves at the endpoints are

$$\mathbf{b}^{(k)}(0) = \frac{n!}{(n-k)!} \Delta^k \mathbf{b}_0 \quad (30)$$

$$\mathbf{b}^{(k)}(1) = \frac{n!}{(n-k)!} \Delta^k \mathbf{b}_{n-k} \quad (31)$$

where the Δ forward differences are defined as

$$\Delta^j \mathbf{b}_i = \Delta^{j-1} \mathbf{b}_{i+1} - \Delta^{j-1} \mathbf{b}_i \quad (32)$$

for $j = 1, 2, \dots$ and $\Delta^0 \mathbf{b}_i = \mathbf{b}_{i+1} - \mathbf{b}_i$. These allow us to compute the control points directly from the raw derivatives.

Let $\mathbf{m}_i^{(k)}, i = 0, 1$ denote the appropriate k -th directional derivatives at the two endpoints of the boundary curve. Then from requiring

$$\mathbf{m}_i^{(k)} = \mathbf{b}^{(k)}(i) \quad , (i = 0, 1) \quad (33)$$

to hold, we have

$$\mathbf{m}_0^{(k)} = \frac{n!}{(n-k)!} \Delta^k \mathbf{b}_0 \quad (34)$$

$$\mathbf{m}_1^{(k)} = \frac{n!}{(n-k)!} \Delta^k \mathbf{b}_{n-k} \quad (35)$$

This allows us to progressively compute the control points from the derivatives such that the resulting curve will reconstruct them at the endpoints.

For example, the first three derivatives at $t = 0$ determine the $\mathbf{b}_1, \mathbf{b}_2, \mathbf{b}_3$ control points from

$$\mathbf{m}_0^{(1)} = n(\mathbf{b}_1 - \mathbf{b}_0) \quad (36)$$

$$\mathbf{m}_0^{(2)} = n(n-1)(\mathbf{b}_2 - \mathbf{b}_1 - \Delta \mathbf{b}_0) \quad (37)$$

$$\mathbf{m}_0^{(3)} = n(n-1)(n-2)(\mathbf{b}_3 - \mathbf{b}_2 - \Delta \mathbf{b}_1 - \Delta^2 \mathbf{b}_0) \quad (38)$$

as

$$\mathbf{b}_1 = \frac{\mathbf{m}_0^{(1)}}{n} + \mathbf{b}_0 \quad (39)$$

$$\mathbf{b}_2 = \frac{\mathbf{m}_0^{(2)}}{n(n-1)} + \Delta \mathbf{b}_0 + \mathbf{b}_1 \quad (40)$$

$$\mathbf{b}_3 = \frac{\mathbf{m}_0^{(3)}}{n(n-1)(n-2)} + \Delta^2 \mathbf{b}_0 + \Delta \mathbf{b}_1 + \mathbf{b}_2 \quad (41)$$

and at $t = 1$ endpoint from

$$\mathbf{m}_1^{(1)} = n(\mathbf{b}_n - \mathbf{b}_{n-1}) \quad (42)$$

$$\mathbf{m}_1^{(2)} = n(n-1)(\Delta \mathbf{b}_{n-1} - \mathbf{b}_{n-1} + \mathbf{b}_{n-2}) \quad (43)$$

$$\begin{aligned} \mathbf{m}_1^{(3)} &= n(n-1)(n-2)(\Delta^2 \mathbf{b}_{n-2} - \Delta^2 \mathbf{b}_{n-3}) \\ &= n(n-1)(n-2)(\Delta^2 \mathbf{b}_{n-2} - \Delta \mathbf{b}_{n-2} + \mathbf{b}_{n-2} - \mathbf{b}_{n-3}) \end{aligned} \quad (44)$$

as

$$\mathbf{b}_{n-1} = \mathbf{b}_n - \frac{\mathbf{m}_1^{(1)}}{n} \quad (45)$$

$$\mathbf{b}_{n-2} = \mathbf{b}_{n-1} - \Delta \mathbf{b}_{n-1} + \frac{\mathbf{m}_1^{(2)}}{n(n-1)} \quad (46)$$

$$\mathbf{b}_{n-3} = \mathbf{b}_{n-2} - \Delta \mathbf{b}_{n-2} + \Delta^2 \mathbf{b}_{n-2} - \frac{\mathbf{m}_1^{(3)}}{n(n-1)(n-2)} \quad (47)$$

References

- [1] D. Barath, T-J. Chin, O. Chum, D. Mishkin, R. Ranftl, and J. Matas. RANSAC in 2020 tutorial. In *CVPR*, 2020. 6
- [2] D. Barath and J. Matas. Graph-cut RANSAC. In *CVPR*, pages 6733–6741, 2018. 1, 2
- [3] D. Barath and J. Matas. Progressive-X: Efficient, anytime, multi-model fitting algorithm. In *ICCV*, pages 3780–3788, 2019. 1
- [4] D. Barath, J. Noskova, M. Ivashechkin, and J. Matas. MAGSAC++, a fast, reliable and accurate robust estimator. In *CVPR*, 2020. 1, 2, 3
- [5] D. Barath, J. Noskova, and J. Matas. MAGSAC: marginalizing sample consensus. In *CVPR*, 2019. <https://github.com/danini/magsac>. 1, 2, 3
- [6] Z. Cai, T-J. Chin, and V. Koltun. Consensus maximization tree search revisited. In *ICCV*, pages 1637–1645, 2019. 2
- [7] D. P. Capel. An effective bail-out test for RANSAC consensus scoring. In *BMVC*, 2005. 2
- [8] O. Chum and J. Matas. Randomized RANSAC with tdd test. In *BMVC*, volume 2, pages 448–457, 2002. 2
- [9] O. Chum and J. Matas. Matching with PROSAC-progressive sample consensus. In *CVPR*. IEEE, 2005. 2
- [10] O. Chum and J. Matas. Optimal randomized RANSAC. *TPAMI*, 30(8):1472–1482, 2008. 2, 5
- [11] O. Chum, J. Matas, and J. Kittler. Locally optimized ransac. In *Joint Pattern Recognition Symposium*. Springer, 2003. 1

- [12] G. Farin. *Curves and Surfaces for Computer Aided Geometric Design (3rd Ed.): A Practical Guide*. Academic Press Professional, Inc., San Diego, CA, USA, 1993. 4
- [13] M. A. Fischler and R. C. Bolles. Random sample consensus: a paradigm for model fitting with applications to image analysis and automated cartography. *Communications of the ACM*, 1981. 1
- [14] A. W. Fitzgibbon. Simultaneous linear estimation of multiple view geometry and lens distortion. In *CVPR*, volume 1, pages I–I. IEEE, 2001. 5
- [15] D. Ghosh and N. Kaabouch. A survey on image mosaicking techniques. *Journal of Visual Communication and Image Representation*, 2016. 1
- [16] R. Hartley and A. Zisserman. *Multiple view geometry in computer vision*. Cambridge university press, 2003. 3
- [17] H. Isack and Y. Boykov. Energy-based geometric multi-model fitting. *IJCV*, 2012. 1
- [18] M. Ivashechkin, D. Barath, and J. Matas. VSAC: Efficient and accurate estimator for h and f. 2021. 2, 8
- [19] Z. Kukulova, J. Heller, M. Bujnak, and T. Pajdla. Radial distortion homography. In *CVPR*, pages 639–647, 2015. 8
- [20] H. M. Le, T-J. Chin, A. Eriksson, T-T. Do, and D. Suter. Deterministic approximate methods for maximum consensus robust fitting. *TPAMI*, 2019. 2
- [21] K. Lebeda, J. Matas, and O. Chum. Fixing the locally optimized RANSAC. In *BMVC*. Citeseer, 2012. 1
- [22] D. G. Lowe. Object recognition from local scale-invariant features. In *ICCV*. IEEE, 1999. 6
- [23] J. Matas and O. Chum. Randomized RANSAC with sequential probability ratio test. In *ICCV*, volume 2, pages 1727–1732. IEEE, 2005. 2
- [24] J. Matas, O. Chum, M. Urban, and T. Pajdla. Robust wide-baseline stereo from maximally stable extremal regions. *IVC*, 2004. 1
- [25] D. Mishkin, J. Matas, and M. Perdoch. MODS: Fast and robust method for two-view matching. *CVIU*, 2015. 1
- [26] K. Ni, H. Jin, and F. Dellaert. GroupSAC: Efficient consensus in the presence of groupings. In *ICCV*, pages 2193–2200. IEEE, 2009. 2
- [27] T. T. Pham, T-J. Chin, K. Schindler, and D. Suter. Interacting geometric priors for robust multimodel fitting. *TIP*, 2014. 1
- [28] F. Pomerleau, F. Colas, and R. Siegwart. A review of point cloud registration algorithms for mobile robotics. *Foundations and Trends in Robotics*, 4(1):1–104, 2015. 3
- [29] P. Pritchett and A. Zisserman. Wide baseline stereo matching. In *ICCV*. IEEE, 1998. 1
- [30] R. Raguram, O. Chum, M. Pollefeys, J. Matas, and J-M. Frahm. USAC: a universal framework for random sample consensus. *TPAMI*, 2013. 2
- [31] A. Ricci. A Constructive Geometry for Computer Graphics. *The Computer Journal*, 16(2):157–160, May 1973. 4
- [32] J. Schönberger, E. Zheng, M. Pollefeys, and J-M. Frahm. Pixelwise view selection for unstructured multi-view stereo. In *ECCV*, 2016. 1
- [33] J. L. Schönberger and J-M. Frahm. Structure-from-motion revisited. In *CVPR*, 2016. 1
- [34] C. Sminchisescu, D. Metaxas, and S. Dickinson. Incremental model-based estimation using geometric constraints. *TPAMI*, 2005. 1
- [35] P. H. Torr, S. J. Nasuto, and J. M. Bishop. NAPSAC: High noise, high dimensional robust estimation—it’s in the bag. 2002. 2
- [36] P. H. S. Torr. Bayesian model estimation and selection for epipolar geometry and generic manifold fitting. *IJCV*, 2002. 2
- [37] P. H. S. Torr and D. W. Murray. Outlier detection and motion segmentation. In *Optical Tools for Manufacturing and Advanced Automation*. International Society for Optics and Photonics, 1993. 1
- [38] P. H. S. Torr and A. Zisserman. MLESAC: A new robust estimator with application to estimating image geometry. *CVIU*, 2000. 2, 3
- [39] P. H. S. Torr, A. Zisserman, and S. J. Maybank. Robust detection of degenerate configurations while estimating the fundamental matrix. *CVIU*, 1998. 1
- [40] Lloyd N. Trefethen. *Approximation Theory and Approximation Practice*. SIAM, 2012. 4
- [41] E. Trulls, Y. Jun, K. Yi, D. Mishkin, J. Matas, and P. Fua. Image matching challenge. In *CVPR*, 2020. 6
- [42] Abraham Wald. *Sequential analysis*. Courier Corporation, 2004. 2
- [43] J. Xiao, K. A. Ehinger, A. Oliva, and A. Torralba. Recognizing scene viewpoint using panoramic place representation. In *CVPR*, 2012. 8
- [44] J. S-C. Yuan. A general photogrammetric method for determining object position and orientation. *Transactions on Robotics and Automation*, 5(2):129–142, 1989. 3
- [45] M. Zuliani, C. S. Kenney, and B. S. Manjunath. The multi-RANSAC algorithm and its application to detect planar homographies. In *ICIP*. IEEE, 2005. 1